System-Level Validation of Radiated Noise Source Characterization Using Only Near-Field Magnitude Information

Ze Sun, *Student Member, IEEE*, Yansheng Wang, *Member, IEEE*, and DongHyun Kim, *Member, IEEE*

***Abstract*—To characterize the radiated noise sources in the radio-frequency interference simulations, a novel equivalent dipole source extraction method was proposed by our group previously. An iteration algorithm and the genetic algorithm work together to reconstruct an equivalent source using near-field magnitude information only while minimizing the number of dipoles needed. In this letter, the previously proposed equivalent dipole extraction algorithm is extended to efficiently extract an equivalent source of harmonics. Furthermore, the algorithm is verified using the actual product instead of simplified test boards. A rigorous and systematic validation process is proposed and conducted, which ensures the robustness and credibility of the extraction algorithm for future applications.**

***Index Terms*—Equivalent dipole reconstruction, radiated noise source characterization, radio frequency interference.**

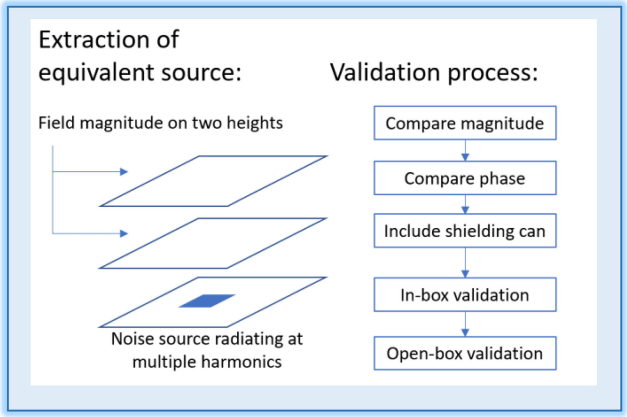

I. Introduction

THE DEVELOPMENT of consumer electronic devices has brought about higher data rates [1], denser component placement [2], and more modules [3] than ever before. Inadequate design can lead to increased susceptibility to desensitization in receivers. To overcome these challenges, simulations are often preferred over measurements [4] since they can detect potential failures in the early stages of product design and enable timely design modifications.

The accuracy of radio-frequency interference (RFI) simulations is influenced by noise source modeling, coupling path modeling, and receiver modeling [5], [6]. This letter focuses on the characterization of radiated noise sources. Numerical simulations are commonly employed to calculate the radiation from the noise source. In most cases, however, the physical structure and driving signal information of the noise source are inaccessible. Therefore, researchers often rely on analyzing the near-field distribution above the source to predict the behavior of the radiator. In [7], the tangential H-field components on an imaginary closed box were measured to calculate the equivalent current distribution. This approach enables the prediction of emission from the actual noise source using Huygens' principle. However, measuring the field distribution across the entire surface of the closed box can be difficult in practice. Another approach to modeling the radiator is to construct equivalent dipole sources from the measured emission [7]. Traditional reconstruction methods require both the magnitude and phase of the near field [8]. However, phase-resolved near-field measurements require an expensive vector network analyzer (VNA), which is unavailable in many radio-frequency (RF) laboratories. Even with a VNA, phase measurement is more challenging than magnitude measurement. To avoid the need for phase measurement, a dipole reconstruction algorithm using magnitude-only information was introduced in [9], but it has limitations in the grid density of the dipole array and accuracy.

Take-Home Messages:

- A novel algorithm for extracting equivalent dipole sources to model radiated noise sources is proposed, which eliminates the need for challenging near-field phase measurement required in other algorithms and minimizes the number of extracted dipoles
- The algorithm is extended to quickly reconstruct the equivalent source at different harmonic frequencies, which is valuable in real-world applications.
- The proposed algorithm is validated through a comprehensive process, including comparing the magnitude and phase of the emission field from the extracted equivalent source with measurement results, modeling surrounding structures in both simulation and measurement, and testing the coupled noise at the victim side.
- The paper provides a rigorous framework to assess and validate the algorithm's performance, paving the way for wider adoption in electromagnetic interference modeling.

Manuscript received 21 June 2023; revised 26 July 2023 and 16 September 2023; accepted 23 October 2023. Date of publication 6 November 2023; date of current version 8 March 2024. This work was supported in part by the National Science Foundation (NSF) under Grant IIP-1916535. *(Corresponding author: Ze Sun.)*

Ze Sun and DongHyun Kim are with the Electromagnetic Compatibility Laboratory, Missouri University of Science and Technology, Rolla, MO 65401 USA (e-mail: sunz1@umsystem.edu; dkim@mst.edu).

Yansheng Wang is with Google LLC, Mountain View, CA 94043 USA (e-mail: yanshengw@google.com).

Digital Object Identifier 10.1109/LEMCPA.2023.3330402

Our prior work [10] proposed a novel radiated noise source extraction algorithm that avoids the phase-resolved near-field measurement and minimizes the number of dipoles. The algorithm employs an iterative approach and a genetic algorithm (GA) to extract the equivalent dipole source based on magnitude-only information while simultaneously optimizing the position of the extracted dipoles. However, this algorithm can only extract equivalent sources at a single frequency. In real applications, noise sources usually radiate at multiple harmonic frequencies, and it is time consuming to reconstruct the equivalent source for each harmonic.

A further drawback of the prior research is the absence of validation. For instance, in [11], a magnetic dipole was utilized to simulate radiation from a microstrip, which was intentionally simplified to make it easy to determine the position and orientation of the equivalent dipole. In [12], the algorithm was validated by only comparing the magnitude of the radiation pattern from the original radiator and the extracted dipoles. The comparison of the phase information is missing. To address this issue, we propose a robust and standardized validation approach. We conducted multiple validations of the proposed algorithm, ranging from the module level to the system level while considering the complex configurations surrounding the noise source and victim antenna in practical products. The results demonstrate a strong correlation between simulation and measurement, indicating that the extracted dipoles can be effectively employed for desense simulations in real-world scenarios.

This letter is organized as follows. In Section II, the algorithm is introduced and extended to extract the equivalent dipole of radiated noise source at different harmonics. The validation approach is then demonstrated in Sections III–VI. Specifically, Section III focuses on the accuracy of reconstructing the phase of the radiated field. Section IV considers the effects of surrounding structures on the emission pattern. Section V compares simulated and measured coupled noise at the victim antenna in a simplified environment. Section VI models coupling in real products. Section VII concludes this letter.

II. Algorithm of Equivalent Source Extraction

An algorithm for extracting equivalent dipole sources of the radiation source at a single frequency using only the magnitude information of the emission field was proposed in [1]. This section reviews the algorithm for completeness and extends its ability to extract equivalent sources at multiple harmonic frequencies.

First, the radiated H field from the emitter is measured. The least-square method (LSM) is then employed to calculate the magnitude and phase of the dipoles, as shown in (1), where T is the transfer function depending on dipole positions and H-field observation points, while X represents reconstructed dipoles

$$X = \left(T'T\right)^{-1}T'H. \tag{1}$$

There are two challenges in obtaining T and H values in (1). First, the structure of the noise source is often unknown, making it challenging to determine the number, position, orientation, and type of dipoles. Consequently, the transfer function T cannot be accurately calculated. Second, LSM requires both H-field magnitude and phase. However, measuring the phase is more difficult than measuring the magnitude.

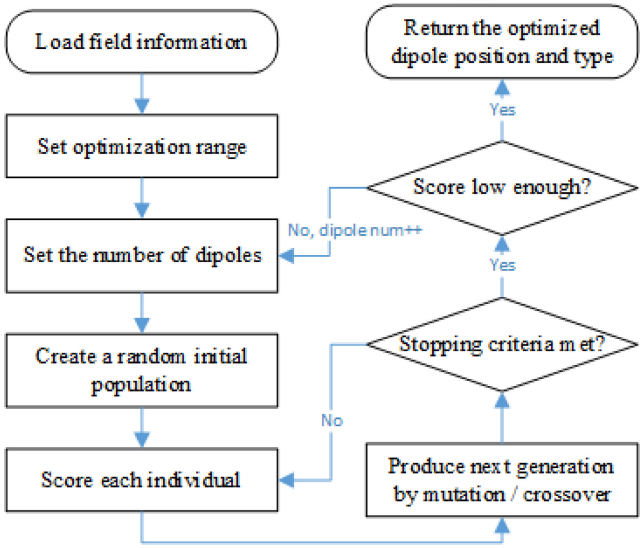

Fig. 1. Workflow of dipole reconstruction.

To address these issues, we proposed a novel equivalent dipole extraction algorithm, as illustrated in Fig. 1. First, near-field scans are performed at two different scanning heights to capture the magnitude distribution of the radiation field. The selected heights must be in proximity to the noise source to ensure that the scanning process captures the majority of radiation within the limited scanning area. At the same time, it is crucial to maintain a certain separation between the two scanning heights to enable accurate phase reconstruction. After loading the measured field magnitude, the GA optimizes the position, orientation, and type of dipoles. The dipole position constraint is based on the physical size of the radiator. The possible set of equivalent dipoles can be positioned anywhere within the 3-D physical dimensions of the noise source. At each optimized position, the dipole can be any of the six candidates, namely, Mx, My, Mz, Px, Py, and Pz.

During each iteration, GA first creates a random initial population. Each individual of the population is a possible set of equivalent dipoles with different positions, orientations, and types. Next, the magnitudes and phases of each individual are reconstructed using the iterative algorithm illustrated in Fig. 2. Here, an artificial field concept is introduced, whereby the magnitude of the artificial field remains the same as the measurement result during the iteration, and the phase is continuously updated. Initially, the phase of fields on two scanning surfaces is set as zero. Next, the magnitudes and phases of dipoles are initialized by substituting the artificial field on surface 2 into (1). Then, the iteration proceeds as follows.

1) Calculate radiation of the current dipole on surface 1.
2) Update the phase of the artificial field on surface 1 with step 1 result, keeping the magnitude of the artificial field unchanged.
3) Update dipole source by substituting using step 2's artificial field into (1).
4) Calculate the radiation of the current dipole on surface 2.
5) Update the phase of the artificial field on surface 2 with step 4 result, keeping the magnitude unchanged.
6) Update dipole source using step 5's artificial field.

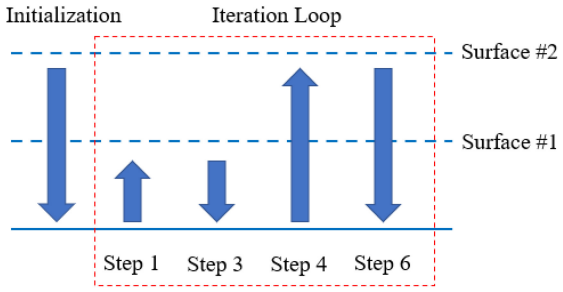

Fig. 2. Iteration process to determine the magnitude and phase of equivalent dipoles.

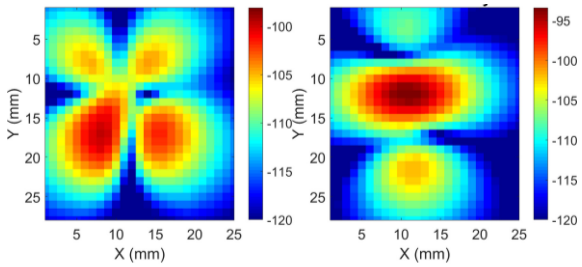

Fig. 3. (a) Measured H_x at 5 mm height. (b) Measured H_y at 5-mm height. Unit: dBA/m.

7) Calculate the radiation from the current dipole on surfaces 1 and 2. Use (2) to obtain the fitness value, where H_x^{meas} and H_y^{meas} are measured H-field magnitudes, and H_x^{fit} and H_y^{fit} are radiated fields from the reconstructed dipole. If the relative error does not converge, repeat the iteration from step 1

$$\text{Fitness} = \sqrt{\frac{\sum\left[\left(|H_x^{\text{meas}}| - |H_x^{\text{fit}}|\right)^2 + \left(|H_y^{\text{meas}}| - |H_y^{\text{fit}}|\right)^2\right]}{\sum\left(|H_x^{\text{meas}}|^2 + |H_y^{\text{meas}}|^2\right)}}. \quad (2)$$

The final fitness value obtained after the iteration is fed back to the GA script. As the individuals within the population have different fitness values, some may initially exhibit significant differences from the desired radiation pattern. The GA script employs a selection process, favoring individuals with lower fitness scores (better fitness) as parents for the next generation. These selected parents are then used to create the subsequent generation through either mutation or crossover operations. The algorithm continuously generates new populations with different dipole locations and types until the stopping criteria are met.

The number of dipoles required for an accurate reconstruction of the radiated noise source is contingent upon the complexity of the noise source being analyzed. The algorithm initiates with a single dipole under optimization. Subsequently, if the resulting reconstruction aligns closely with the near-field scan data, the algorithm terminates. Conversely, if the correlation falls below the specified threshold, the number of dipoles under optimization is increased incrementally, and the optimization process is iterated. This iterative approach continues until the final reconstruction closely matches the near-field scan results.

To demonstrate the effectiveness of the proposed algorithm, the radiation pattern of an image sensor found in cell phones is

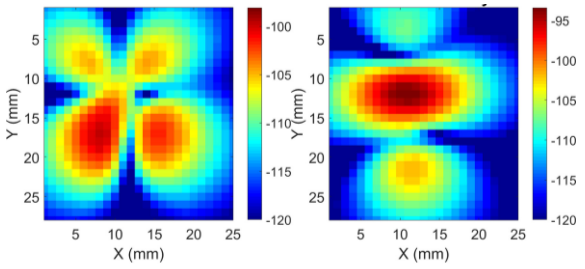

Fig. 4. (a) Radiated H_x from reconstructed dipoles at 5-mm height. (b) Radiated H_y from reconstructed dipoles at 5 mm height. Unit: dBA/m.

characterized, as detailed in [10]. The image sensor efficiently radiates at the master clock (M-clk) harmonic frequencies. The H-field pattern at 648 MHz is measured using a near-field scanner with Rohde & Schwarz FSVA40 signal analyzer (SA) and costum-designed H-field probe at 3 and 5 mm, with results presented in Fig. 3. The scanning step size is 1 mm in both the x and y axes. The maximum values of H_x and H_y fields are -98.1 and -93.4 dBA/m, respectively. Three dipoles are required to reconstruct the radiated noise source, and the radiation from them is displayed in Fig. 4, with maximum H_x and H_y field values of -99.7 and -93.3 dBA/m, respectively. The reconstructed field distribution and maximum values agree well with the measurements.

To fully evaluate the victim antenna degradation due to the image sensor, equivalent dipole sources must be extracted at different harmonic frequencies. One way to do this is to repeat the proposed procedure for each frequency separately, which can be time consuming due to multiple GA optimizations. An alternative strategy is to reconstruct dipole sources at other frequencies based on single-frequency extraction results. In this letter, radiation at 624, 648, 672, and 696 MHz, four M-clk harmonics between 600 and 700 MHz were investigated as an example. Fig. 5 shows near-field scan results above the radiator at these frequencies. The assessment of field distribution similarity across different harmonics is quantified using (2). Given the consistent nature of the radiator's current distribution across all harmonic frequencies, it follows that the resulting field distributions at these harmonics exhibit a notable degree of similarity. Thus, it is reasonable to assume equivalent dipole sources at these frequencies share the same position and type, and the only differences are the magnitude and phase of each dipole.

Using this assumption, equivalent dipoles at other harmonic frequencies are reconstructed. First, the H-field distribution at these frequencies is measured, the results are shown in Fig. 5. Second, the reconstructed dipole position and type at 648 MHz are loaded into the script. With known dipole position and type, the time-consuming GA optimization is skipped. The back-and-forth iteration algorithm determines the dipole magnitude and phase at each frequency, which varies due to minor field distribution differences.

The emission patterns from the reconstructed dipoles at the three frequencies of interest are presented in Fig. 6. The maximum values of the measured and reconstructed fields are summarized in Table I, and good agreement between the two is observed. Notably, the extraction script omits the time-consuming GA optimization process. Once the equivalent source at one harmonic frequency is extracted, determining

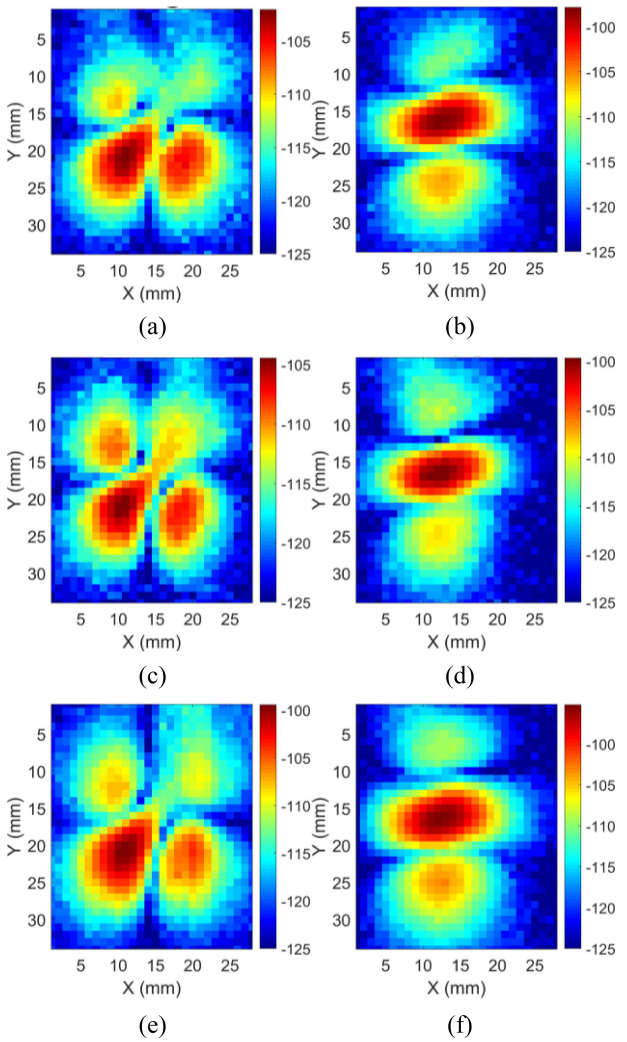

Fig. 5. Measured field distribution when the scanning height is 3 mm. (a) H_x at 624 MHz. (b) H_y at 624 MHz. (c) H_x at 672 MHz. (d) H_y at 672 MHz. (e) H_x at 696 MHz. (f) H_y at 696 MHz. The unit is dBA/m.

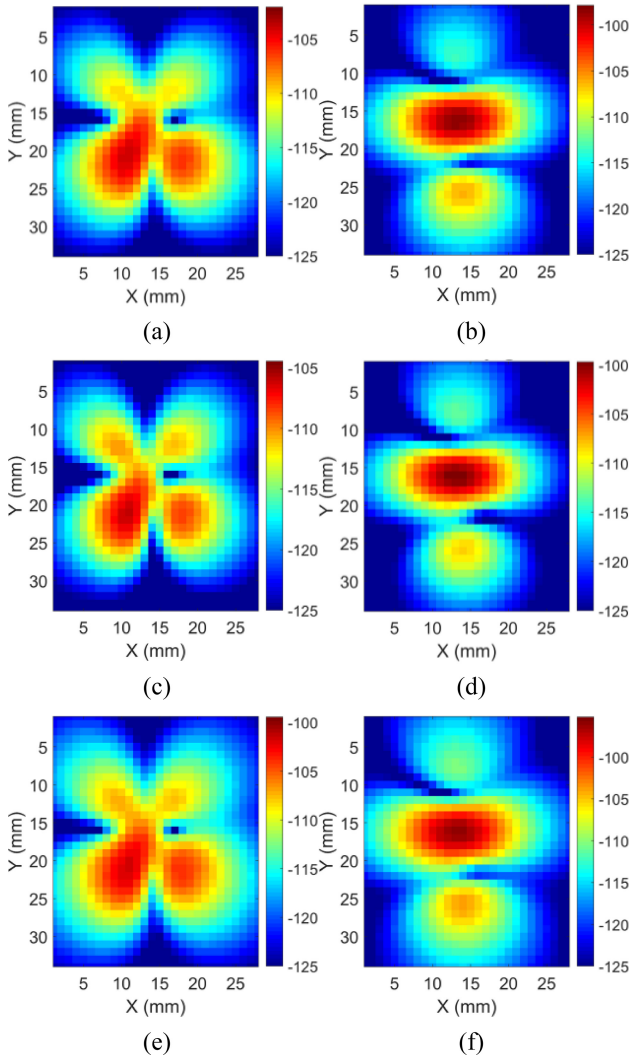

Fig. 6. Emission field from extracted equivalent dipoles. (a) H_x at 624 MHz. (b) H_y at 624 MHz. (c) H_x at 672 MHz. (d) H_y at 672 MHz. (e) H_x at 696 MHz. (f) H_y at 696 MHz. The unit is dBA/m.

TABLE I
MAXIMUM VALUE OF MEASURED AND RECONSTRUCTED FIELDS

Frequency (MHz)	624	648	672	696
Measured Hx (dBA/m)	-102.1	-97.8	-104.4	-99.4
Measured Hy (dBA/m)	-97.8	-93.6	-99.7	-95.2
Reconstructed Hx (dBA/m)	-103.9	-99.7	-106.0	-101.6
Reconstructed Hy (dBA/m)	-98.3	-93.6	-99.7	-95.8

equivalent dipoles at other harmonics becomes straightforward. Besides, when importing equivalent dipoles into the full-wave model for desense simulations, the setup process is simplified, as the dipole position and type remain constant across all simulation frequencies.

III. EMISSION PHASE CORRELATION

The reconstruction results in Section II demonstrate good agreement in the field magnitude between reconstructed and measured fields, serving as an initial step to validate the equivalent source's accuracy. However, it remains unclear whether the phase of the reconstructed field corresponds with the original emission, which is crucial for the accuracy of the desense simulation.

The H-field emissions from the radiator can be measured using the setup depicted in Fig. 7. The Agilent E5071C VNA operates in the tune receiver mode, where both ports serve as receivers. The first port connects to a scanning probe used to capture the radiator's emission, with the probe's position precisely controlled by a scanning robot. The VNA's second port connects to a stationary reference probe, capturing emissions from the traces carrying the M-clk signal in the flex printed-circuit board (FPCB). The phase of the radiation from the image sensor is calculated as the relative difference between these two ports' results.

The phase distributions of the H field at 648 MHz obtained from the measurement and the reconstructed dipole are presented in Figs. 8 and 9, respectively. In the color maps of these figures, red corresponds to $+180°$ while blue represents $-180°$, which are equivalent angles in the polar coordinate system. The reconstructed dipole's phase field is in good

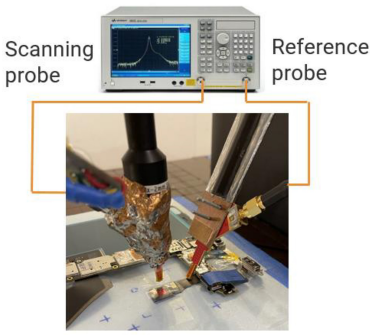

Fig. 7. H-field phase measurement setup.

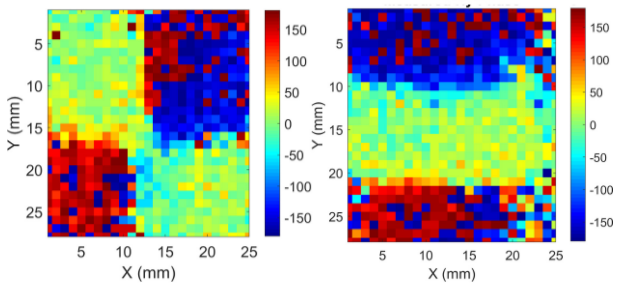

Fig. 8. (a) Measured H_x phase distribution. (b) Measured H_y phase distribution. Unit: degrees.

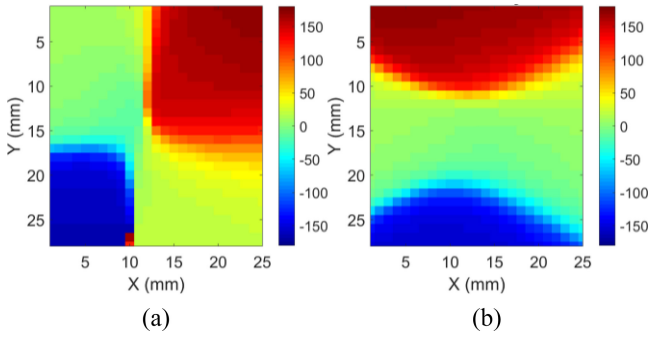

Fig. 9. (a) H_x phase distribution from reconstructed dipoles. (b) H_y phase distribution from reconstructed dipoles. Unit: degrees.

agreement with the measurement data, and the measurement noise is reduced in the reconstruction result. This result demonstrates that, despite not having prior knowledge of the phase information, the proposed equivalent dipole reconstruction algorithm accurately reproduces the emission's magnitude and phase from extracted dipoles.

IV. Modeling of Radiator With Shielding Can

In practical applications, metal shielding is commonly employed to enclose radiated noise sources, significantly altering the emission pattern from the radiator and the coupled power at the victim antenna. Therefore, in addition to ensuring the magnitude and phase distribution of the field from the equivalent source correlate well with the unshielded radiator, it is crucial to verify the effectiveness of the equivalent dipoles when metal shielding is introduced.

First, the radiation from a shielded camera module, as illustrated in Fig. 10, is measured using near-field scanning. Due to the increased height introduced by the shielding can

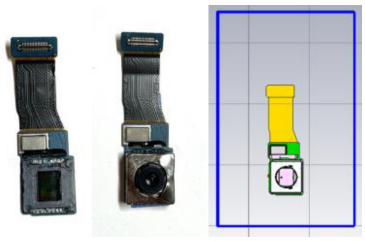

Fig. 10. (from left to right): Unshielded image sensor, shielded camera module, and simulation model of the shielded camera module.

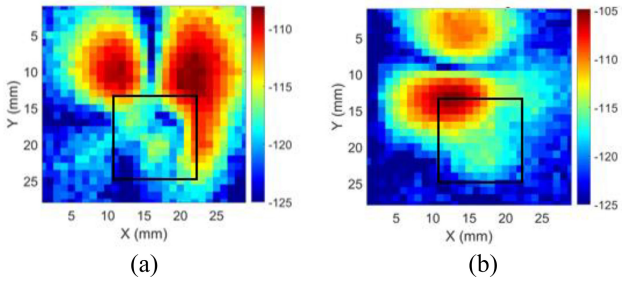

Fig. 11. (a) H_x-field distribution above shielded camera module. (b) H_y-field distribution above shielded camera module. Unit: dBA/m.

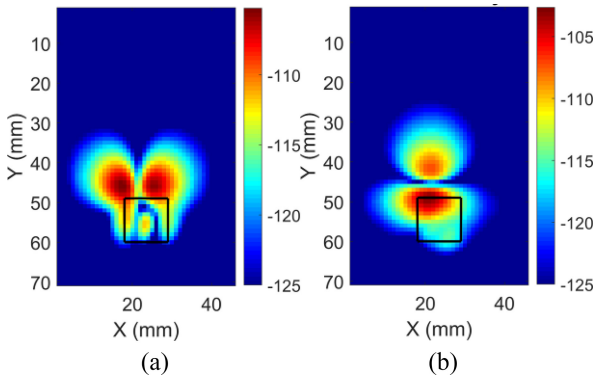

Fig. 12. (a) Simulated H_x-field distribution above shielded camera module. (b) Simulated H_y-field distribution above shielded camera module. Unit: dBA/m.

and lens, the scanning height is raised to 7 mm above the ground. Fig. 11 displays the measurement results at 648 MHz. The maximum field strengths of H_x and H_y are -108.1 and -104.8 dBA/m, respectively. Comparing these results with the field pattern from an unshielded image sensor (Fig. 3) reveals a dramatic change in the hotspot shape.

Next, the emission from the shielded camera is simulated using the model shown in Fig. 10. The equivalent dipoles, reconstructed based on the emission from the unshielded image sensor, are placed inside the shielding can, which is constructed according to the actual structure. Detailed information about the image sensor structure is not required, as the dipole source can imitate its radiation. The blue box surrounding the model denotes the region of the field monitor. Fig. 12 exhibits the simulated emission, with the black box in the middle representing the position of the rectangular shielding. The maximum values of the simulated H_x and H_y fields are -105.3 and -102.7 dBA/m, respectively. The hotspot shape and the maximum value of the radiation field in the simulation are in good agreement with the measurement results. Consequently, the extracted equivalent source can be

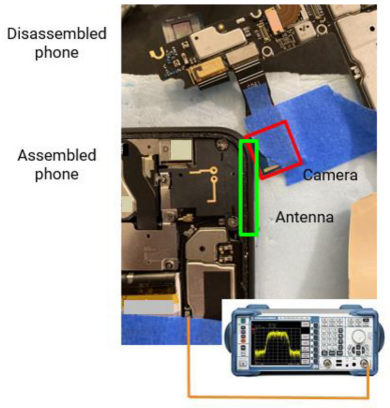

Fig. 13. In-box validation measurement setup.

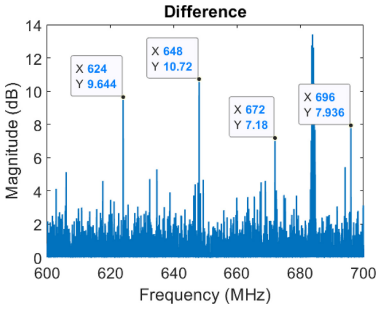

Fig. 14. Difference in the coupled noise when the camera is turned on or off in the in-box validation.

employed to predict the emission field when the original radiator is shielded, which is essential for practical applications. This phenomenon can be explained by the physical meaning of the equivalent dipoles: the M-clk current distribution inside the image sensor remains unchanged after the addition of the shielding can, so the previously reconstructed dipoles continue to function.

V. In-Box Validation

The strong correlation of field patterns between the measurements and simulations demonstrated in previous sections does not necessarily guarantee that the coupled power at the victim port can be accurately predicted by the reconstructed source, which is the ultimate goal of desense simulation. Therefore, further validation of the equivalent dipoles through in-box and open-box validation is necessary.

In in-box desense measurements, both the radiator and the victim antenna are placed inside a controlled environment that isolates them from external factors, such as electromagnetic interference, ambient noise, or physical disturbances. In our case, the measurement setup is shown in Fig. 13. The shielded camera module serves as the radiator, with the LTE antenna of another phone positioned nearby as the victim. An SA measures the coupled noise at the antenna port in the 600–700-MHz range, with the camera turned off and on. The difference between these two spectra is shown in Fig. 14. Even with the shielding can in place, strong coupled noise persists at M-clk harmonic frequencies (e.g., 624, 648, and 696 MHz) when the camera is in close proximity to the antenna.

The corresponding simulation model for calculating coupled noise is shown in Fig. 15. In this simulation, the camera shielding can structure and equivalent dipoles are positioned next to the victim antenna, ensuring that their relative positions

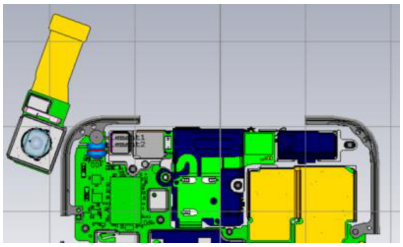

Fig. 15. Simulation model of noise coupling from shielded camera to nearby antenna. The imported dipole moments are underneath the shielding can.

TABLE II
In-Box Correlation

Frequency (MHz)	Measurement (dBm)	Simulation (dBm)
624	-115.6	-116.5
648	-109.5	-111.0
672	-115.6	-117.9
696	-116.2	-115.3

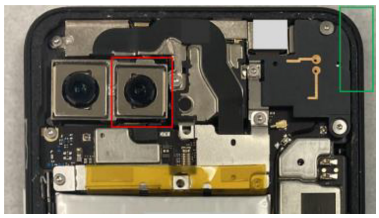

Fig. 16. Cell phone under test.

match those in the measurement setup. For different harmonic frequencies, the corresponding dipoles are imported, and the coupled noise is calculated separately. Table II lists the simulation results. At all four harmonic frequencies, the simulation results exhibit good agreement with the measurement data, indicating the original radiator is accurately modeled using the equivalent dipole source and that surrounding structures do not impact modeling accuracy.

VI. Open-Box Validation

The in-box validation simplifies the transmission of the noise from the radiator to the victim. To further verify the accuracy of the reconstructed source, the most effective way is to measure the coupling between the aggressor and victim in real-world applications, a process known as open-box validation. In this setup, the shielded camera module is placed inside a phone, and the coupled noise at the LTE antenna is measured. The phone used in the measurement is depicted in Fig. 16. During the measurement, the camera module enclosed in the red box is activated, and the coupled noise received by the LTE antenna placed in the green box is measured using an SA. The difference between the measured spectra when the camera is turned off and on is shown in Fig. 17. As the distance between the camera and the antenna is significantly greater than in the previous in-box measurement, no clear peaks are observed at the M-clk harmonic frequencies.

The corresponding simulation model is presented in Fig. 18, with the extracted dipoles positioned inside the shielding can. At 648 MHz, the calculated noise at the LTE antenna port is −130.7 dBm, which is below the noise floor of the measurement result. This outcome aligns with the study's expectation that the coupled noise would be below the noise floor, resulting in no clear peaks observed in the measured

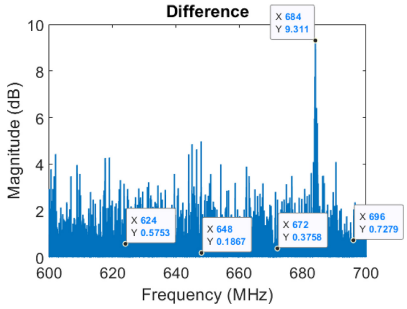

Fig. 17. Difference in the coupled noise when the camera is turned on or off in the open-box validation.

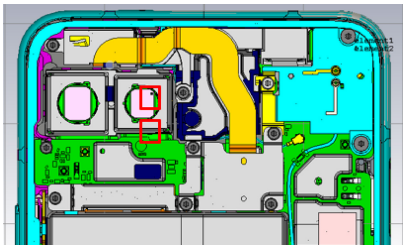

Fig. 18. Simulation model of the cell phone under test. The red boxes indicate the position where the dipoles are located.

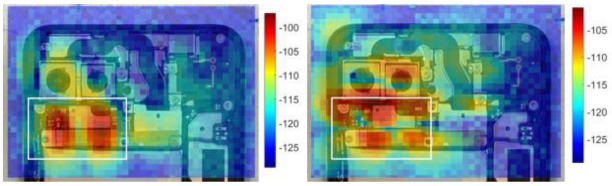

Fig. 19. Measured H-field distribution above the phone. (a) H_x. (b) H_y. The unit is dBA/m. The white box indicated the position of the connector.

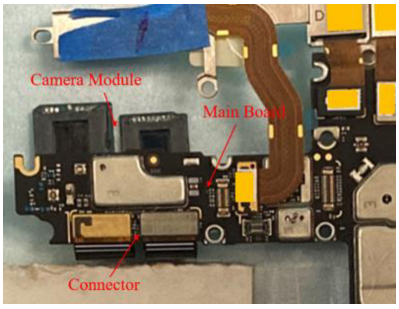

Fig. 20. Main board and the camera module used in the near-field scan. The camera modules are wrapped to imitate the configuration of the real phone.

spectrum. However, this comparison does not fully validate the proposed model.

To validate the proposed modeling method, a stronger radiator than the camera module is needed. It was found that the board-to-board (B2B) connector between the camera flex and the main board effectively radiates at 684 MHz when measuring the H-field emission above the phone. The corresponding field distributions are shown in Fig. 19, where the maximum values of H_x and H_y are -97.1 and -101.0 dBA/m, respectively. The coupled noise at the LTE antenna port is measured to be -118.5 dBm. Therefore, the B2B connector is chosen to validate the proposed method by constructing its equivalent source and comparing the simulated and measured coupled noise at the victim antenna port.

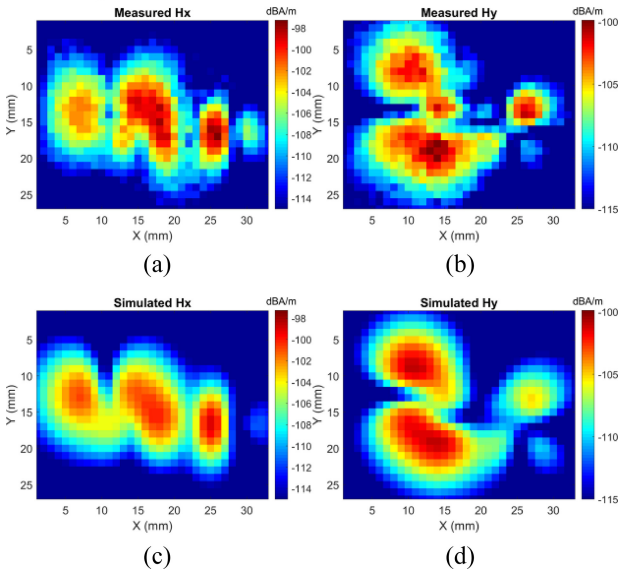

Fig. 21. Measured field distribution. (a) Measured H_x at 684 MHz. (b) Measured H_y at 684 MHz. (c) Reconstructed H_x at 684 MHz. (d) Reconstructed H_y at 684 MHz.

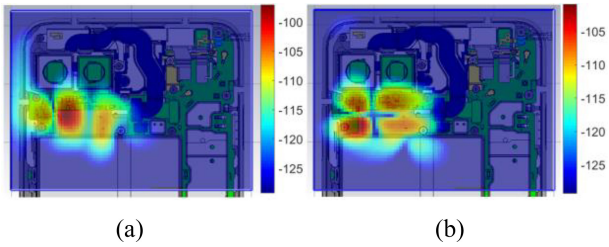

Fig. 22. Simulated emission from the reconstructed source. (a) H_x. (b) H_y. The unit is dBA/m.

Following the radiated noise modeling process proposed in Section II, the H-field emission from the connector is measured first. As illustrated in Fig. 20, a near-field scan is performed using only the main board and the camera module, rather than the assembled cell phone. This approach ensures that the extracted dipole source reflects only the emission from the connector, excluding the influence of surrounding structures. The measured field patterns from a scanning height of 5 mm are presented in Fig. 21(a) and (b). After loading the measurement data into the equivalent source extraction script, the radiation from the resulting dipoles is depicted in Fig. 21(c) and (d). The reconstructed field distribution closely resembles the measurement result.

Next, the extracted dipoles are imported into the phone's full-wave simulation model. The simulated H-field emission is displayed in Fig. 22. The maximum values of H_x and H_y are -97.3 and -101.5 dBA/m, respectively. Compared with the measurement result in Fig. 19, both the position of the hot spot and the maximum emission value demonstrate good agreement. Furthermore, the coupled noise at the antenna port is simulated, resulting in -116.2 dBm, which is close to the measurement data (-118.5 dBm). This finding suggests that the extracted dipoles can be used to model radiated noise sources in real products.

VII. Conclusion

Building upon our previous work, this letter presents a novel method for extracting equivalent dipole sources to model the radiated noise source in desense simulations. By employing a GA and an iterative approach, we eliminate the challenging near-field phase measurement required in other equivalent dipole extraction algorithms and minimize the number of extracted dipoles. Furthermore, we extend the algorithm to quickly reconstruct the equivalent source at different harmonic frequencies, which is valuable in real-world applications.

In addition, this letter introduces a comprehensive step-by-step validation process for the proposed algorithm. First, the magnitude of the emission field from the extracted equivalent source is compared with the measurement result. Next, the phase of the field from the simulation needs to be closely aligned with the measurement. Then, the surrounding structures near the radiator, such as metal shielding, need to be included in both the simulation and measurement, as they can significantly alter the emission pattern. Furthermore, the in-box validation creates a simplified environment to quickly test the coupled noise at the victim side. Finally, the open-box validation verifies the accuracy of the equivalent source in real-world applications. By providing a rigorous framework to assess and validate the algorithm's performance, our work ensures its reliability and paves the way for wider adoption in the electromagnetic interference modelings.

References

[1] S. Choi et al., "Estimation and analysis of crosstalk effects in high-bandwidth memory channel," in *Proc. IEEE Int. Symp. Electromagn. Compat./Asia–Pacific Symp. Electromagn. Compat. (EMC/APEMC)*, 2018, p. 4.

[2] D.-H. Kim et al., "Through-silicon via capacitance–voltage hysteresis modeling for 2.5-D and 3-D IC," *IEEE Trans. Compon., Packag. Manuf. Technol.*, vol. 7, no. 6, pp. 925–935, Jun. 2017.

[3] W. Zhang et al., "System-Level EMI of an artificial router system with multiple radiators: Prediction and validation," *IEEE Trans. Electromagn. Compat.*, vol. 62, no. 4, pp. 1601–1610, Aug. 2020.

[4] Y. Zhong et al., "Measurement-based quantification of buzz noise in wireless devices," in *Proc. Joint Int. Symp. Electromagn. Compat. Sapporo Asia–Pacific Int. Symp. Electromagn. Compat. (EMC Sapporo/APEMC)*, 2019, pp. 552–555.

[5] Q. Huang, Y. Liu, L. Li, Y. Wang, C. Wu, and J. Fan, "Radio frequency interference estimation using transfer function based dipole moment model," in *Proc. IEEE Int. Symp. Electromagn. Compat. IEEE Asia–Pacific Symp. Electromagn. Compat. (EMC/APEMC)*, May 2018, pp. 115–120.

[6] Y. Wang, S. Wu, J. Zhang, Z. Yang, K. Wu, and J. Fan, "A simulation-based coupling path characterization to facilitate desense design and debugging," in *Proc. IEEE Symp. Electromagn. Compat., Signal Integr. Power Integrity (EMC, SI, PI)*, Jul. 2018, pp. 150–155.

[7] C. Wu, Z. Sun, Q. Huang, Y. Wang, J. Fan, and J. Zhou, "A method to extract physical dipoles for radiating source characterization and near field coupling estimation," in *Proc. IEEE Int. Symp. Electromagn. Compat., Signal Power Integr. (EMC+ SIPI)*, 2019, pp. 580–583.

[8] Y. Wang et al., "Correcting antenna pattern in offset measurements based on equivalent dipole moments," in *Proc. IEEE Symp. Electromagn. Compat., Signal Integrity Power Integr. (EMC, SI, PI)*, Jul. 2018, pp. 493–498.

[9] J. Zhang and J. Fan, "Source reconstruction for IC radiated emissions based on magnitude-only near-field scanning," *IEEE Trans. Electromagn. Compat.*, vol. 59, no. 2, pp. 557–566, Apr. 2017.

[10] Z. Sun, Y. Wang, W. Lee, K. Wu, and D. Kim, "Radiated noise source characterization based on magnitude-only near field," in *Proc. IEEE Int. Joint EMC/SI/PI EMC Europe Symp.*, Jul. 2021, pp. 376–380.

[11] Q. Huang et al., "Reciprocity theorem based RFI estimation for heatsink emission," in *Proc. IEEE Int. Symp. Electromagn. Compat., Signal Power Integr. (EMC+ SIPI)*, Jul. 2019, pp. 590–594.

[12] J.-R. Regue, M. Ribo, J.-M. Garrell, and A. Martin, "A genetic algorithm based method for source identification and far-field radiated emissions prediction from near-field measurements for PCB characterization," *IEEE Trans. Electromagn. Compat.*, vol. 43, no. 4, pp. 520–530, Nov. 2001.